Materials Characterization 145 (2018) 389–401

Contents lists available at ScienceDirect

Materials Characterization

journal homepage: www.elsevier.com/locate/matchar

Plastic flow and microstructural instabilities during high-pressure torsion of Cu/ZnO composites

Yuanshen Qi[a,*], Anna Kosinova[a], Askar R. Kilmametov[b], Boris B. Straumal[b,c,d], Eugen Rabkin[a,*]

[a] Department of Materials Science and Engineering, Technion – Israel Institute of Technology, 32000 Haifa, Israel
[b] Karlsruhe Institute of Technology, Institute of Nanotechnology, Eggenstein-Leopoldshafen, Germany
[c] National University of Science and Technology MISIS, Moscow, Russia
[d] Institute of Solid State Physics, Scientific Center in Chernogolovka, Russian Academy of Sciences, Chernogolovka, Russia

ARTICLE INFO

Keywords:
High-pressure torsion
Heterogeneous material
Hydrodynamic instability
Abnormal grain growth
Superplastic ceramic nanoparticle
Co-deformation

ABSTRACT

We conducted high-pressure torsion (HPT) of hybrid materials composed of two copper disks with a layer of ZnO ceramic nanoparticles sandwiched in-between. A detailed microstructural analysis of the processed samples revealed a surprisingly high level of plastic deformation introduced in individual ZnO particles, even though they possess a much high hardness than the surrounding Cu. Moreover, we demonstrated that by tailoring the initial geometry of the system (i.e. introducing holes in the cladding Cu disks), we can effectively change the flow mode of ZnO particle clusters from laminar to turbulent one and facilitate their deagglomeration process. Finally, the presence of ZnO particles decreased the microstructural stability of the Cu matrix. We discussed the obtained results in terms of hydrodynamic and microstructural instabilities during plastic deformation. This work expands our understandings of the cooperative severe plastic deformation of two dissimilar materials and sheds new light on the design of hybrid materials.

1. Introduction

The conventional design strategy of strong metal-based materials for structural applications usually relies upon uniform distribution of reinforcement phases in a homogenous matrix [1]. However, recent studies have demonstrated that heterogeneous microstructures can offer several advantages over their homogeneous counterparts. The heterogeneity could be obtained by either the change of defects densities and arrangements in a single phase metal [2,3], or the combination and patterning of different phases [4–6]. With proper microstructure "architecturing" and nanostructuring, strength and ductility can be enhanced simultaneously in the heterogeneous structure as a result of postponed deformation localization and extended strain hardening [7,8]. To achieve this, utilization of innovative processing routes and microstructural design methods are essential.

As pointed out by Bouaziz et al. [4,9], substantial breakthroughs in the development of the heterogeneous architectured materials could be achieved by incorporating the refinement of material building blocks with the aid of severe plastic deformation (SPD) techniques. Indeed, SPD techniques including equal-channel angular pressing [10–12], high-pressure torsion [13–24], accumulative roll-bonding [25–29], etc. have been drawing increasing attention due to their ability to combine intensive components intermixing with the simultaneous nanostructuring of the individual building constituents [5,30].

The co-deformation of individual building blocks modifies the initial material on both macro- and microscopic length scales. On one hand, under the plastic flow the individual building constituents would go through a series of geometrical and size changes, such as de/agglomeration, de/bonding, fracture and solid-state welding. On the other hand, the microstructures inside each constituent would undergo refinement resulting from the hydrostatic pressure and shear straining. Therefore, by controlling the SPD processing parameters of the multicomponent material such as the amount of strain [11,12], strain rate, strain path, processing temperature [10] and post-deformation heat treatment [31], the balance between architecturing, alloying and nanostructuring can be manipulated.

In the past decade, it was demonstrated that processing of multicomponent materials by high-pressure torsion (HPT) results in extensive microstructure refinement and components intermixing. Sauvage et al. demonstrated that surprisingly high degree of mechanical alloying between Cu and Fe in a filamentary composite was achieved due to significantly enhanced atomic mobility and

* Corresponding authors.
E-mail addresses: yuanshen.qi@technion.ac.il (Y. Qi), anna.kosinova@technion.ac.il (A. Kosinova), askar.kilmametov@kit.edu (A.R. Kilmametov), straumal@issp.ac.ru (B.B. Straumal), erabkin@technion.ac.il (E. Rabkin).

https://doi.org/10.1016/j.matchar.2018.09.001
Received 14 July 2018; Received in revised form 31 August 2018; Accepted 2 September 2018
Available online 04 September 2018

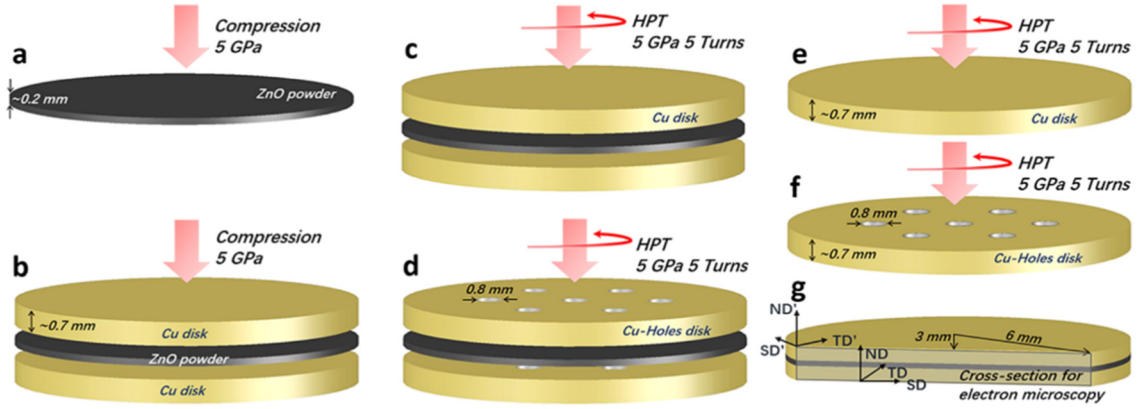

Fig. 1. The schematic illustration of the processing and characterization scheme. (a, b) compression at 5 GPa without torsion of the ZnO powder and Cu-ZnO sample; (c, d) HPT processing of the Cu-ZnO and Cu-Holes-ZnO samples; (e, f) HPT processing of the Cu and Cu-Holes samples, for the reference; (g) the cross-section where electron microscopy characterization was performed. Note the difference between the coordinate systems (ND, SD, TD) and (ND′, SD′, TD′).

interdiffusion [13]. Bachmaier et al. found that by changing the strain route and increasing the strain, transformation from ultrafine grained two-phase composite to nanostructured supersaturated solid solution alloy occurred in a Cu/Fe powder mixture in a two-step HPT process [14]. The exceptional chemical intermixing at room temperature between powders was also utilized for producing ultrahigh-strength W-based nanocomposites. As stated by Edalati et al. [15], HPT process produced strong interfaces by interdiffusion bonding and avoided chemical reactions that occur at elevated temperature. However, recent studies demonstrated that intermetallic and even amorphous phases can form during HPT process as well. In Oh-Ishi et al. work, a hybrid disk consisting of two separate Al and Cu half-disks was processed by HPT and intermetallic phases were formed, accompanied by the formation of supersaturated Al- and Cu-based solid solutions [16]. Using the same two half-disk arrangement, Sun et al. have recently shown that after 20 HPT rotations, amorphization would occur in the Cu/Zr and Cu/Ag couples [18]. Kawasaki et al. [19–22] conducted a series of investigations on HPT-processed Al-Mg-Al disks which were stacked together in a sandwich-like manner. After processing, heterogeneous microstructure was formed with ultrafine multi-layered structure in the central region of the disk and a nano-layered intermetallic phase embedded in the nanostructured Al matrix near the edge of the disk. Sandwich structure was also studied in Rogachev et al. work by employing steel-V alloy-steel configuration [23]. Lower HPT processing temperature was found to be more effective for the mixing of two phases. This is a result of a delicate interplay between the plastic deformation-induced intermixing and defects annihilation during HPT [32–36]. Most recently, Sun et al. conducted HPT of a mixture of cryomilled Al and Ti powders and found that the intermetallic phases formed after just one rotation, even though some Ti particles were not fragmented yet and appeared to retain their original shape [17].

As summarized above, most of the previous studies of the effect of HPT on heterogeneous materials were focused on the mixtures of powders, or a combination of two kinds of bulk metals. The focus of the present study is on a composite structure with a particulate ceramic layer sandwiched between two disks of a bulk metal. In addition to the scientific significance, such configuration may also provide a new way of controllable distribution of ceramic particles in metallic matrix and concomitant stabilization of nanoscale microstructure. To this end, the composite of Cu disk - ZnO nanopowder - Cu disk was chosen for this study. It is worth noting that finely dispersed ZnO particles on Cu substrate serve as an efficient catalyst for CO_2 hydrogenation to methanol [37].

In our previous study, it has been found that the existence of prefabricated holes dramatically changes the plastic flow behavior during HPT of pure Cu [38]. In the holed disk the material tended to flow inwards and close the holes rather than outwards as in the case of solid Cu disk. In the present study we also drilled the holes in the Cu disks of the Cu/ZnO/Cu sandwich, with the aim of affecting the degree of intermixing between the ZnO particles and the Cu matrix. All in all, in the present work we processed by the HPT and characterized by various electron microscopy techniques four different types of samples: Cu disk/ZnO nanopowder/Cu disk sandwich, holed Cu disk/ZnO nanopowder/holed Cu disk sandwich, monolithic Cu disk, and holed Cu disk. The latter two samples served as a reference, to investigate the effect of ZnO nanoparticles on the microstructure evolution and plastic flow in Cu matrix.

2. Experimental Methods

The Cu material of an ultrahigh purity of 99.9995 wt% (5N5) and nodular-shaped ZnO of an purity of 99.999% were employed in this study. The Cu disks cut from the as-cast ingot for further HPT processing were of 10 mm in diameter and 0.7 mm in thickness (in what follows “Cu disks”). In several Cu disks seven cylindrical holes of 0.8 mm in diameter were drilled through the thickness (in what follows, “Cu-Holes disks”). One hole was located at the center of the disk while the other six were located about 2.5 mm away from the disk center and 60° away from each other. Seven holes resulted in a nominal porosity of 4.48%. Two kinds of sandwich-like samples were processed by HPT. One was Cu-ZnO-Cu disk (in what follows, “Cu-ZnO disk”), and the other one was Cu-Holes-ZnO-Cu-Holes disk (in what follows, “Cu-Holes-ZnO disk”).

The high-pressure torsion processing and compression were all conducted on a Bridgman anvil-type unit with a quasi-constrained die using a custom-built computer controlled HPT device (W. Klement GmbH, Lang, Austria), and the processing scheme is shown in Fig. 1. First of all, to evaluate the effect of shear straining on the evolution of ZnO particles in terms of their average size and distribution, two compression tests with the pressure of 5 GPa without rotation were conducted on the ZnO nanopowder and on the Cu-ZnO disk, see Fig. 1(a, b). Then, the HPT processing (5 GPa compressive pressure, 5 anvil rotations at a rotation rate of 1 revolution per minute) was carried out on both sandwich samples, Cu-ZnO disk and Cu-Holes-ZnO disk, as shown in Fig. 1(c, d). At last, the HPT was also performed on Cu and Cu-Holes disks for reference.

The microstructure characterization was conducted on the cross-section area of the disks in Fig. 1(b–f). In what follows we assigned the labels normal direction (ND), shearing direction (SD), and transverse direction (TD) to the disk normal, to the in-plane direction in the cross-section orthogonal to ND, and to the out-of-cross-section direction, respectively (see Fig. 1(g)). It should be noted, however, that the true

shearing and transverse directions (SD′ and TD′) are the tangential and radial directions which change with respect to the location of the characterized regions. After processing, the disk was cut 3 mm away from its center and two Cu plates with similar size were glued on each side of the sample. It is worth noting that after HPT 5 rotations under the pressure of 5 GPa, the microstructure of Cu samples of conventional purity should be homogeneous throughout the sample, both in radial and axial directions [39]. Epoxy was used for glue and the curing was conducted on a hot plate at 120 °C for 20 min. Conventional grinding using SiC paper down to 4000 grit and final mechanical polishing using 50 nm Al_2O_3 suspension were conducted. Final electropolishing was carried out at room temperature in 14 M phosphoric acid by applying electric potential of 1.2 V. Time of about 2 min was sufficient to remove the damaged surface layer and reveal the grains. After electropolishing the samples were rinsed with distilled water. High resolution scanning electron microscopy (HRSEM), electron backscattered diffraction (EBSD) and on-axis transmission Kikuchi diffraction (TKD) measurements were carried out on a Zeiss Ultra Plus SEM equipped with a Bruker EBSD/TKD system. For calculation of average grain size, twins and subgrains defined by the low angle grain boundaries (LAGBs) with misorientation angle below 15° were not accounted for as individual grains. Moreover, average grain size was calculated based on area weight fraction, instead of number fraction. Focused ion beam (FIB) regular cross-section milling was carried out on a FEI Helios NanoLab DualBeam G^3. Transmission electron microscopy (TEM) and scanning transmission electron microscopy (STEM) were performed on Tecnai T20 and Titan Cubed Themis G^2 300, respectively. Energy-dispersive X-ray spectroscopy (EDX) mapping was carried on STEM using a Dual-X detector (Bruker).

3. Results

We characterized the distribution and size of the ZnO clusters in the as-compressed Cu-ZnO disk, and the HPT-processed Cu-ZnO and Cu-Holes-ZnO disks. We also determined the grain size distribution and crystallographic orientations of the grains, paying special attention to the regions in the vicinity of ZnO clusters. They are expected to influence the microstructure evolution of the soft Cu phase due to the strain gradient induced by the hard ceramic particles.

3.1. Evolution of ZnO Clusters and Particles

The cross-section SEM views of the as-compressed Cu-ZnO disk, and of the HPT-processed Cu-ZnO and Cu-Holes-ZnO disks are shown in Fig. 2. Weak bonding between the individual ZnO particles, and between the ZnO particles and Cu in the as-compressed sample resulted in a loss of most of the ZnO material during the sample preparation handling, i.e. cutting and grinding. The hollow middle layer with a uniform thickness in Fig. 2a exemplifies the layer of ZnO particles in the as-compressed state which was lost during sample preparation. In addition, due to the material outflow under the compressive pressure of 5 GPa, scattered ZnO clusters with lower thickness were found at the edge of the disk. This indicates that material flow and relative sliding between the individual ZnO particles enhances adhesion. Indeed, after the HPT process, the bonding strength was significantly increased and ZnO clusters were still embedded in the Cu matrix after the sample preparation, as seen in Fig. 2(b, c). In addition, the overview in Fig. 2(b, c) and enlarged views in Fig. 2($b_{1–4}$) and ($c_{1–4}$) reveal that the HPT-processed Cu-Holes-ZnO exhibited more homogenous distribution and finer sizes of ZnO clusters than the HPT-processed Cu-ZnO disk. The enlarged views in Fig. 2($b_{1–4}$) and ($c_{1–4}$) were taken from locations at increasing distances from the center of the disk. The equivalent von Mises strain ε_{eq} in these locations can be estimated by $\varepsilon_{eq} = 2\pi rN/t\sqrt{3}$, where r, N and t are the distance from the center of the disk, the number of rotations and the thickness of the disk, respectively [40,41]. It is worth noting that the large ZnO cluster is located at the lower surface close to the disk center, as seen in the enlarged view in Fig. 2b_1. This ZnO cluster initially trapped between two equally thick Cu disks "migrated" through to the Cu layer and arrived at the sample bottom. In the magnified images in Fig. 2(c), small vortex-like ZnO clusters can be seen; their formation is related to the plastic flow of Cu and probably is a consequence of plastic flow instability [42].

To statistically evaluate the deagglomeration and redistribution of ZnO clusters in the two HPT-processed Cu-ZnO composite disks, the dimensions of the clusters along the SD and ND have been measured, see Fig. 3. In both cases, there was a clear correlation between the cluster sizes along the shearing and normal axes, i.e. the shorter the cluster in shearing axis, the narrower the clusters in the normal axis. This indicates that increasing extent of stretching of the ZnO clusters also means the higher possibility for them to fracture and deagglomerate. For the Cu-ZnO disk, the size distribution of ZnO clusters was directly influenced by the equivalent strain distribution. Large ZnO clusters were in the center region and their sizes decreased gradually when moving towards the edge regions. In contrast, in the Cu-Holes-ZnO disk, the variations of the cluster sizes were smaller. This indicates that, in general, the plastic deformation was more homogeneous in Cu-Holes-ZnO disk than in the Cu-ZnO disk. Thus, the convective flow of ZnO clusters became also uniform. We suggest that the Cu flow leading to the closure of the pre-existing holes interfered with the simple shear flow and caused more uniform distribution of ZnO clusters. In other words, a fraction of ZnO particles was squeezed into the pre-existing holes. Finally, it is worth noting that since the scatter of clusters dimensions was large (for example, the dimensions for clusters in Cu-ZnO sample along shearing axis ranged from 31 to 421 μm), the standard deviations were larger than their average values.

Apart from the evolution of the ZnO clusters, their building blocks - ZnO nanoparticles - were also influenced by the HPT process and deformed along shearing directions. As seen in Fig. 4, the as-received ZnO particles were nodular in shape [43] and had an average size of 351 ± 174 nm. The compression at 5 GPa caused only insignificant changed of their shape and average size (332 ± 213 nm), even though the hardness of ZnO was reported to be 2–5 GPa [44–46]. In addition, the average size of ZnO particles embedded in the Cu disks and compressed at 5 GPa decreased to 288 ± 201 nm, and the particles elongated along shearing direction (Fig. 4c). In Fig. 2(b, b_1), it can be seen that some ZnO particles were transported to the external surface after HPT of the Cu-ZnO disk. These particles were also characterized from normal direction, see Fig. 4d. Interestingly, their size did not change significantly (334 ± 140 nm). This indicates that the residual ZnO particles trapped between the Cu disk and the anvil evolved by sliding and rotation rather than by plastic deformation and fracture.

The plastic flow of Cu around ZnO clusters was essential for the co-deformation of ZnO particles, as seen in Fig. 4($e_{1–4}$) and ($f_{1–4}$). After the HPT processing, the embedded ZnO particles were extensively deformed and elongated along shearing direction. To determine the influences of the strain level on the extent of their deformation, ZnO particles at four different locations, starting from the disk center [Fig. 4(e_1, f_1)] and at the distances of 1.5 mm (e_2, f_2), 3 mm (e_3, f_3), and 4.5 mm (e_4, f_4) away from the center, were characterized. The length and the thickness (along the ND) of the ZnO particles were measured (Fig. 5). In the case of HPT-processed Cu-ZnO disk, ZnO particles were increasingly stretched along shearing direction with increasing amount of strain. Their average dimension along shearing and normal directions changed from 410 ± 160 nm and 90 ± 50 nm at the disk center to 920 ± 190 nm and 40 ± 10 nm at the disk edge. On the contrary, for HPT-processed Cu-Holes-ZnO disk, the variation of ZnO particles size measured along shearing direction was less significant. The decease of dimensions in normal directions was steady, from 80 ± 30 nm to 40 ± 10 nm (see Fig. 4f_1–f_4). This means that the ZnO particle size of about 1 μm in the shearing direction corresponds to the saturation plateau in the dependence of particle dimension on imposed strain. This trend reflected the increasing strain level from the center to the edge. It

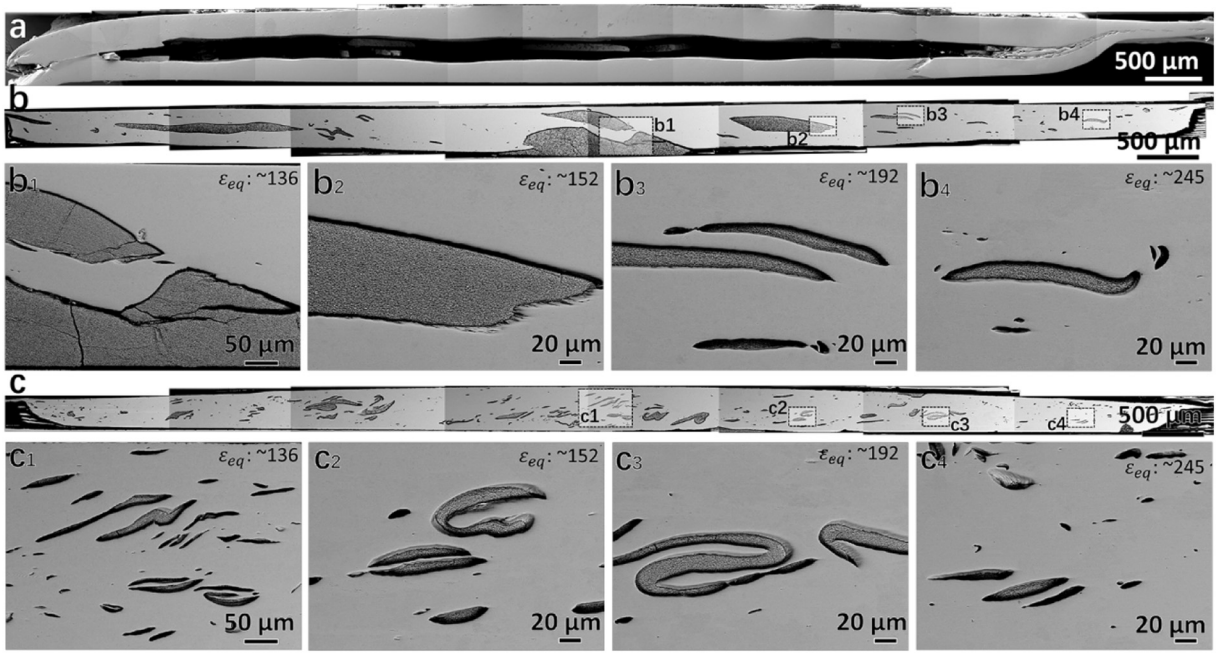

Fig. 2. SEM characterization of the distribution of ZnO clusters in cross-sections. (a) the as-compressed Cu-ZnO disk; (b) the HPT-processed Cu-ZnO disk; (c) the HPT-processed Cu-Holes-ZnO disk. (b_{1-4}) and (c_{1-4}) show the detailed morphology of the ZnO clusters at different locations with the labelled equivalent von Mises strain - ε_{eq}.

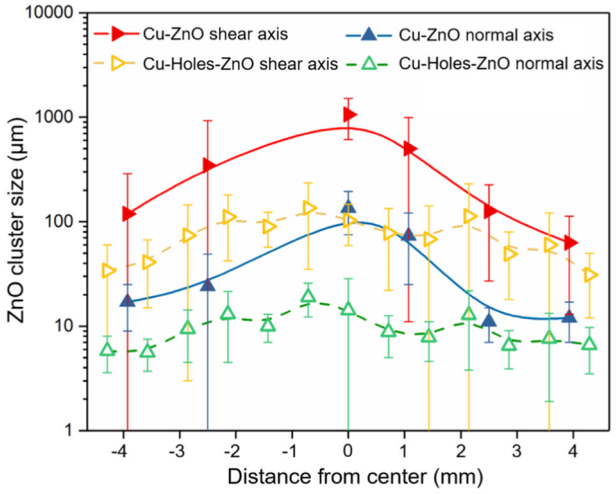

Fig. 3. ZnO cluster size distribution in HPT-processed Cu-ZnO and Cu-Holes-disks.

is evident that in the HPT-processed Cu-Holes-ZnO disk the ZnO particles were extensively deformed even in the center region. Finally, the deagglomeration of ZnO clusters was accompanied by the plastic deformation and fragmentation of the ZnO particles, resulting from the shearing strain.

The morphological evolution of ZnO particles clearly demonstrated the plastic deformation of ceramic particles during HPT when they were embedded in Cu disks. As it can be seen in Fig. 4d, without the constraining pressure, ZnO particles found between the Cu disk and the anvil barely underwent any plastic deformation. This phenomenon is similar to the brittle to ductile transformation of rocks under Earth's mantle [47]. Similar to the metals, the plastic deformation of ceramic particles relies upon defects activity [47–50]. To obtain further insight into the deformation behavior of the ZnO particles, TEM lamella were prepared from the cross-sections of the HPT-processed Cu-ZnO and Cu-Holes-ZnO disks from regions about 4 mm away from the center.

From Fig. 4(e, f), it is clear that the morphology of ZnO particles has transformed from the equiaxed- to flake-shaped. However, from the SEM micrograph, only two dimensions along the ND and SD can be viewed. The TEM micrographs in Fig. 6 show the ZnO particles from transverse direction (TD). Firstly, the widths of ZnO particles from both HPT-processed Cu-ZnO and Cu-Holes-ZnO disks were about 50 nm, which is consistent with the values measured from SEM micrographs. The decrease of the particles height from ~350 nm to ~50 nm implies that they experienced compressive strain of about 87%. Secondly, the measured length of the ZnO flakes was about 3 μm, which means that the volume of the ZnO particles was conserved during HPT processing. Finally, the bright field (BF) TEM micrographs in Fig. 6(c, f) show strong diffraction contrast inside individual ZnO particles, indicating large amount of strain in the form of lattice distortions and dislocations produced by plastic deformation.

To determine preferred deformation texture and the average strain in the ZnO particles, TKD measurements were performed. Fig. 7(a, b) and (e, f) show band contrast (BC) and orientation images of ZnO particles from HPT-processed Cu-ZnO and Cu-Holes-ZnO disks, respectively. From the (0002) and ($10\bar{1}0$) pole figures, Fig. 7(c, g), it can be found that strong texture has developed in both cases, as the maximum intensities were 90 and 60 multiples of random distribution (mrd). Moreover, since in ZnO the basal plane is the easy glide plane compared with the non-basal planes [51,52], its preferred orientation aligned close to the normal direction in both cases, which facilitated the basal slip along transverse and shearing directions. At last, Fig. 7(d, h) presents the misorientation maps for one representative grain in each sample, with the reference point highlighted by a white cross. Significant variations of the in-grain misorientation can be seen in both cases. Peaks in the range of 12° to 16° in both histograms indicated the strong lattice distortion and high density of defects.

To characterize the interface between ZnO cluster and surrounding Cu, one TEM lamella was prepared from the area that included both phases in the HPT-processed Cu-Holes-ZnO disk. The lamella was lifted out from a region about 4 mm away from the center, where the ZnO clusters are very thin in normal direction, 2.5–3.5 μm (see Fig. 8a), in agreement with the observation in Fig. 2c_4. The ZnO nanoparticles of 60 ± 26 nm in size are clearly seen in Fig. 8(a–d), which is also

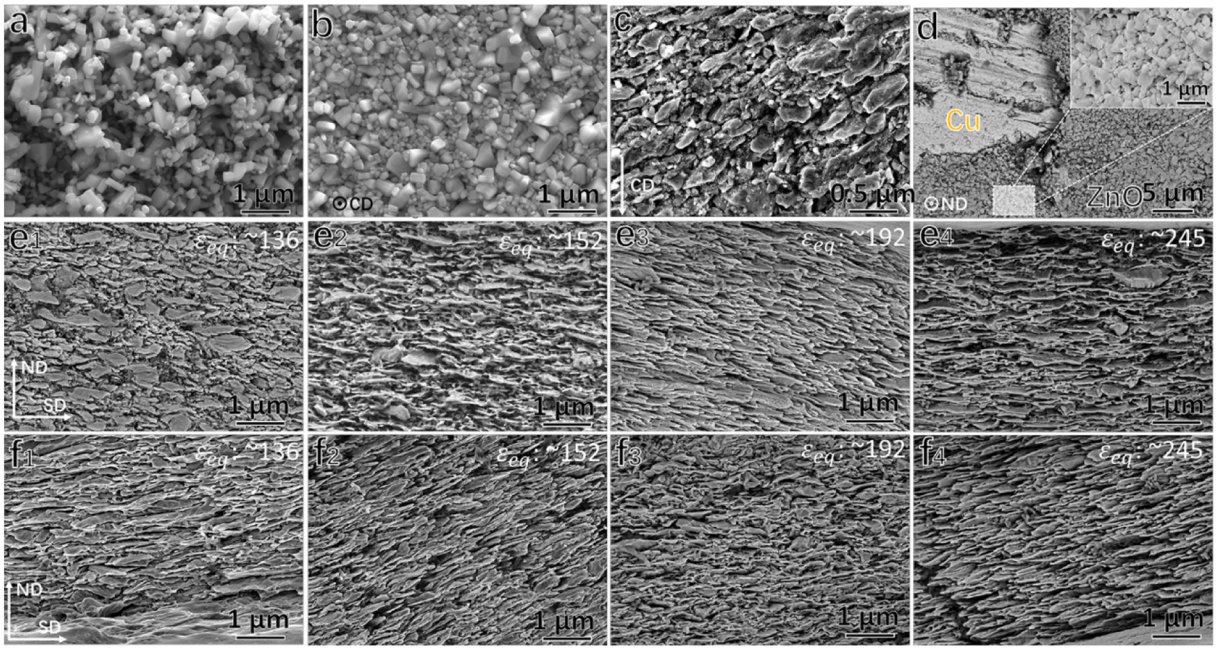

Fig. 4. HRSEM characterization of the ZnO particles at the different deformation stages. (a) as-received ZnO particles, (b) as-compressed ZnO particles, (c) ZnO particles in as-compressed Cu-ZnO disk (d) residual ZnO particles on the external surface of the HPT-processed Cu-ZnO disk, ($e_{1–4}$) and ($f_{1–4}$) embedded ZnO particles in HPT-processed Cu-ZnO and Cu-Holes-ZnO disks, respectively. (e_1, f_1) were taken at the center region, (e_2, f_2), (e_3, f_3) and (e_4, f_4) were taken about 1.5 mm, 3 mm and 4.5 mm away from the center, respectively. For the compressed samples, compression direction (CD) was labelled.

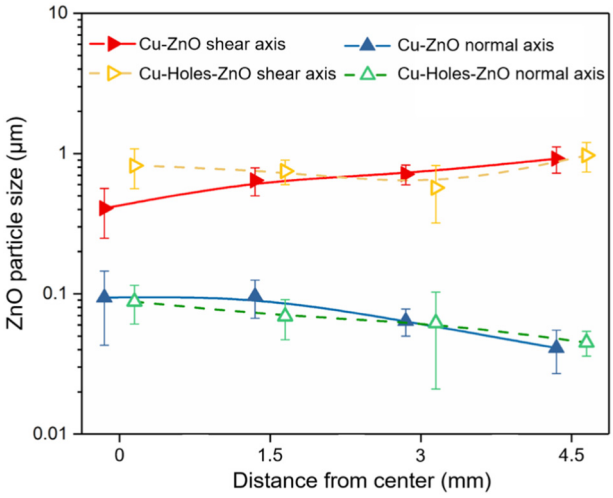

Fig. 5. ZnO particle size distribution in HPT-processed Cu-ZnO disk and Cu-Holes-disk.

consistent with the SEM micrographs in Fig. 4(e_4, f_4). Diffuse grain boundaries between the individual ZnO particles and strong bending contours within the particles can be observed at higher magnification (Fig. 8c), indicating the high strain amplitude and non-equilibrium character of grain boundaries. In addition, the selected-area diffraction pattern (SADP) indicated the presence of only one hexagonal wurtzite phase. Adjacent to the ZnO cluster, layers of ultrafine Cu grains were found on both sides. Relatively clear interior was found in these ultrafine grains, as seen in Fig. 8(b, d). Moreover, the existence of the coarse grains also indicates that the recrystallization and grain growth have occurred in the Cu matrix, probably during holding at room temperature or during the sample preparation stage. To gain deeper understanding of the microstructure of ultrafine grain (UFG) Cu regions abutting the ZnO cluster, the TKD measurement was conducted. The color coded dark field (CCDF) and orientation images of one highlighted Cu grain demonstrate several dislocations in the grain interior, see Fig. 9(a, b). This indicates that recrystallization did not occur in this region, since the grain interior is not dislocation-free and still exhibits lattice distortions. This can also be proved by the grain orientation spread (GOS) image in Fig. 9(c), as the misorientation angle inside one grain varies up to 6°. At the same time, large grains and annealing twins in the coarse grain (CG) regions of Cu clearly indicate that static recrystallization and grain growth have occurred there.

To check whether there was any chemical intermixing or interdiffusion between the Cu and ZnO phases, STEM with EDX mapping was conducted. As seen in Fig. 10(a–c), the interphase boundary between Cu and ZnO is very sharp, indicating the absence of intermixing. Moreover, higher resolution micrographs in Fig. 10(d–f) indicate that neither Zn nor O segregate at the grain boundaries in an abutting UFG Cu matrix, which further proves that interdiffusion did not occur. At last, voids between ZnO particles were seen in the STEM-BF and STEM-high angle annular dark field (HAADF) micrographs (see yellow arrows in Fig. 10(a, b)), indicating the insufficient bonding between them. Therefore, frictional sliding between ZnO particles was another possible deformation mechanism of ZnO particles during HPT.

3.2. Evolution of Cu Grain Structure

Our TKD and (S)TEM-EDX measurements demonstrated that the microstructure of Cu matrix in the vicinity of ZnO clusters is bimodal, with the coexisting regions of the UFGs and CGs. We also demonstrated that the stability of the UFG microstructure near ZnO cluster cannot be attributed to solute segregation at the grain boundaries in Cu or to the particles pinning. To examine the influence of ZnO clusters and holes on the plastic deformation of Cu, we performed extensive EBSD measurements of the Cu matrix in the HPT-processed Cu-ZnO, Cu-Holes-ZnO, Cu, and Cu-Holes disks.

3.2.1. HPT-processed Cu-ZnO

A large-area EBSD mapping was first conducted in order to understand the overall microstructure heterogeneity in HPT-processed Cu-ZnO disk, as presented by the band contrast (BC) image in Fig. 11(a).

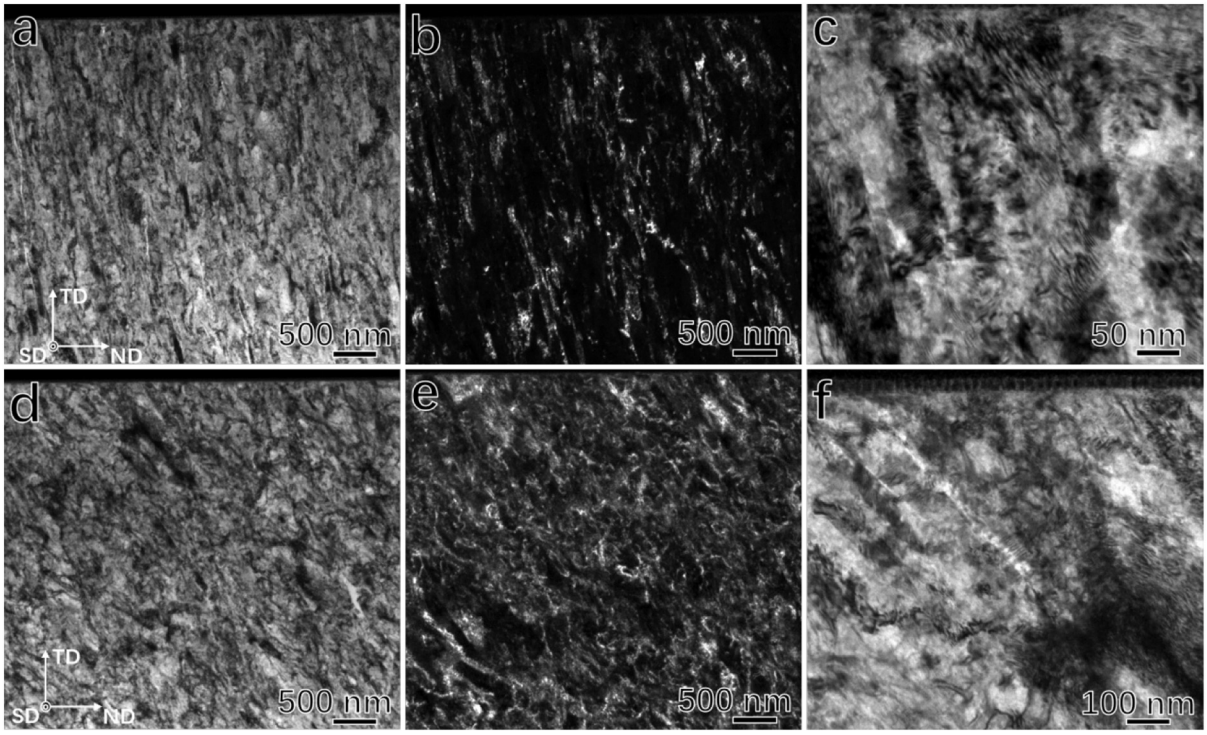

Fig. 6. TEM characterization of HPT-processed ZnO particles from Cu-ZnO (a–c) and Cu-Holes-ZnO (d–f) disks. (a, b) and (d, e) BF and DF TEM images showing the overall morphology of ZnO particles; (c, f) higher magnification BF micrographs showing the defects inside the ZnO particles.

Two regions with different characteristic microstructures were identified: the region within 100 μm from the external surfaces (region A) exhibited bimodal microstructure consisting of the regions of ultrafine and coarse grains (UFGs + CGs). The area in the middle of the disk was dominated by the UFGs (region B). The recrystallization and/or grain growth responsible for the formation of the CGs occurred either during storing the samples at room temperature or during the sample preparation stage (heating to 120 °C for 20 mins for the curing of epoxy), due to low thermal stability of HPT-processed Cu [53,54]. In our previous study of the HPT-processed Cu disk, the layers with bimodal microstructure have been found within 30 μm from the external surfaces [38]. The stability of the UFG component of this bimodal microstructure was attributed to frictional sliding during HPT [38]. The increase in thickness of the layers with bimodal microstructure observed in this study can be rationalized in terms of higher extent of dry sliding between Cu disks and anvils. The extent of sliding increases because of the reinforcing effect of the ZnO clusters on the Cu matrix increasing the overall rigidity of the sandwich samples.

The average size of the CGs measured on the EBSD maps of region A was 37.8 μm, see Fig. 11(b). Moreover, annealing twin lamellae with an average thickness of 0.51 ± 0.3 μm can be clearly seen in Fig. 11(c). The detailed characterization of the UFGs is presented in Fig. 11(d). Their average size is 0.46 μm, which leads to the ratio of about 80 of CG to the UFG sizes. The representative area of the region B is shown in

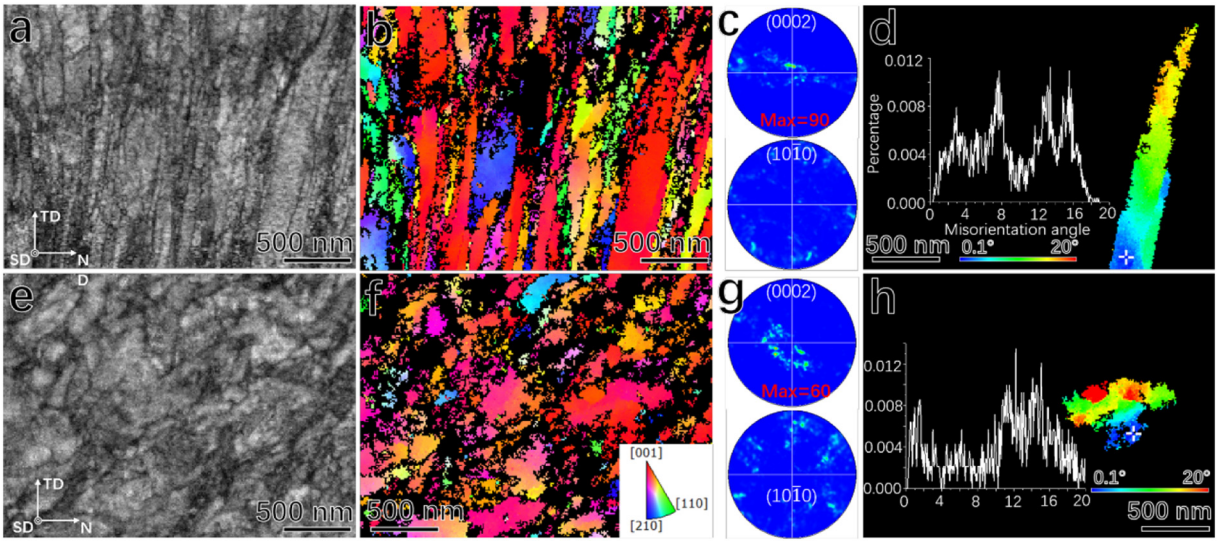

Fig. 7. TKD measurements of ZnO particles from HPT-processed Cu-ZnO (a–d) and Cu-Holes-ZnO disks (e–h). (a, e) BC images; (b, f) orientation images with inserted legend; (c, g) (0002) and (10$\bar{1}$0) PF with maximum intensity labelled; (d, h) misorientation map in one highlighted grain, reference location in the grain is pointed by the white cross; legend and histogram are included.

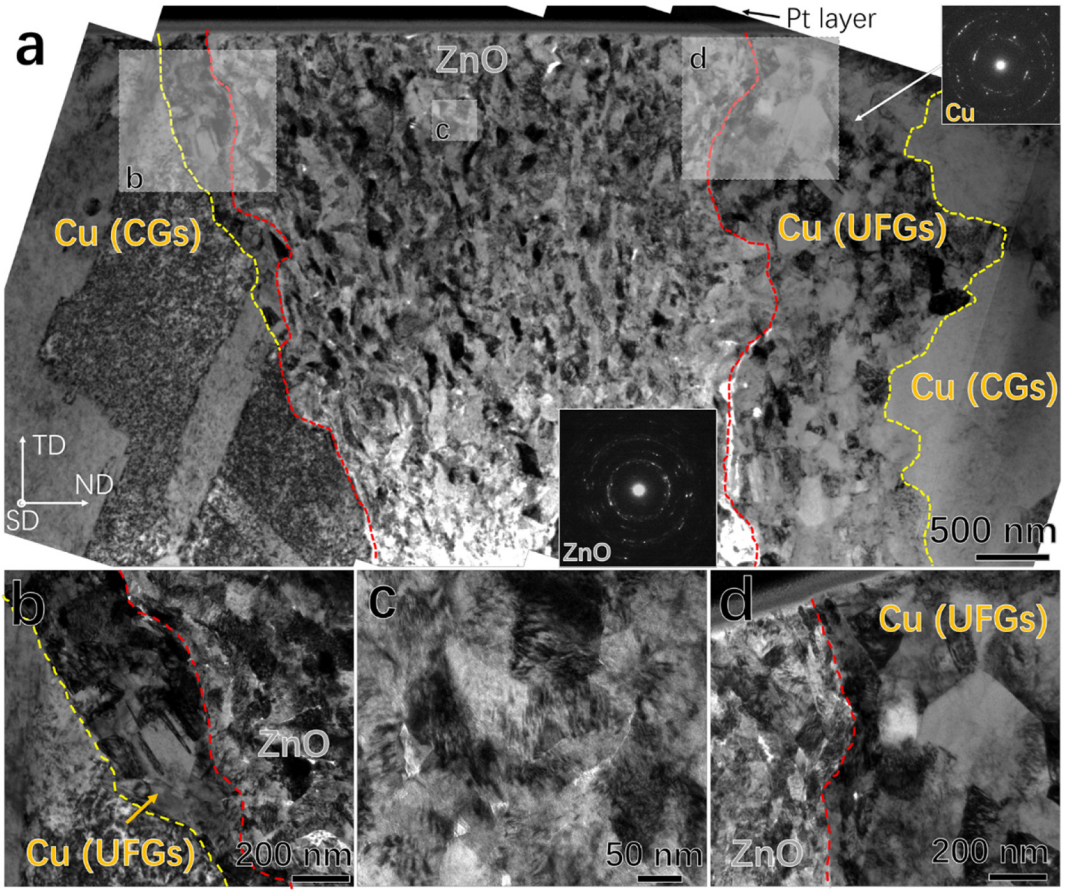

Fig. 8. TEM characterization of ZnO nanoparticles and Cu grains abutting the ZnO cluster. (a) overview showing the interfaces between ZnO and Cu (red dashed lines) and CG/UFG regions of Cu (yellow dashed lines); (b–d) higher magnification micrographs of areas labelled in (a). SADP from ZnO and Cu regions are shown as inserts. (For interpretation of the references to color in this figure legend, the reader is referred to the web version of this article.)

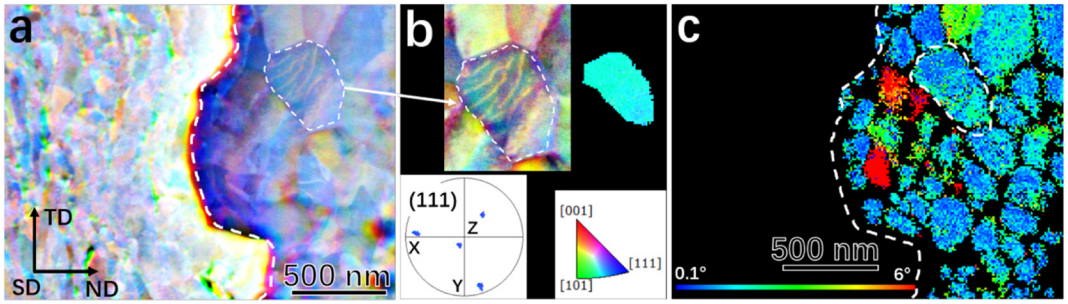

Fig. 9. TKD characterization of Cu grains adjacent to the ZnO cluster. (a) CCDF image; (b) orientation image of the selected Cu grain showing residual dislocations; (c) grain orientation spread image.

Fig. 11(e, f). Compared to the region A, the coarse grains in the region B exhibit smaller average size, around 4.5 μm. This smaller grain size could be related to more homogeneous plastic flow in the region B compared to that in region A, resulting in multiple equivalent nucleation sites for recrystallization during post-processing sample handling. However, the average size of UFGs remained 0.53 μm, similar to that in the Region A. Finally, the GOS image indicates that UFGs exhibit residual strain while their micrometer-sized counterparts are defect free.

3.2.2. HPT-processed Cu-Holes-ZnO

Contrary to the Cu-ZnO disk, only one type of bimodal microstructure was found in the Cu-Holes-ZnO disk (see the overview micrograph in Fig. 12(a)). Both CGs and UFG clusters were present through the thickness of the disk. Based on the microstructure overview, two small regions shown in Fig. 12(b–d) and (e, f) were studied in details. Fig. 12(b–d) show the area located close to the external surface and containing ZnO clusters. The majority of the grains grew extensively and reached the size of about 60 μm, with annealing twin lamellae exhibiting the average thickness of 0.46 ± 0.31 μm, as seen in Fig. 12(b, c). However, UFG clusters embedded between ZnO clusters can be also seen in Fig. 12(d). The UFGs exhibited an average size of 0.46 μm, and results in the ratio of about 120 of the sizes of CGs and the UFGs. The UFG areas related to the pre-existing holes are shown in Fig. 12(e, f). The shear band that is distinguished by its shape and lower indexing rate than the surrounding grains is highlighted in the BC image in Fig. 12(e). The UFGs inside of the shear band are believed to be formed in the healed region of the pre-existing holes. From our previous study, they exhibited high thermal stability due to

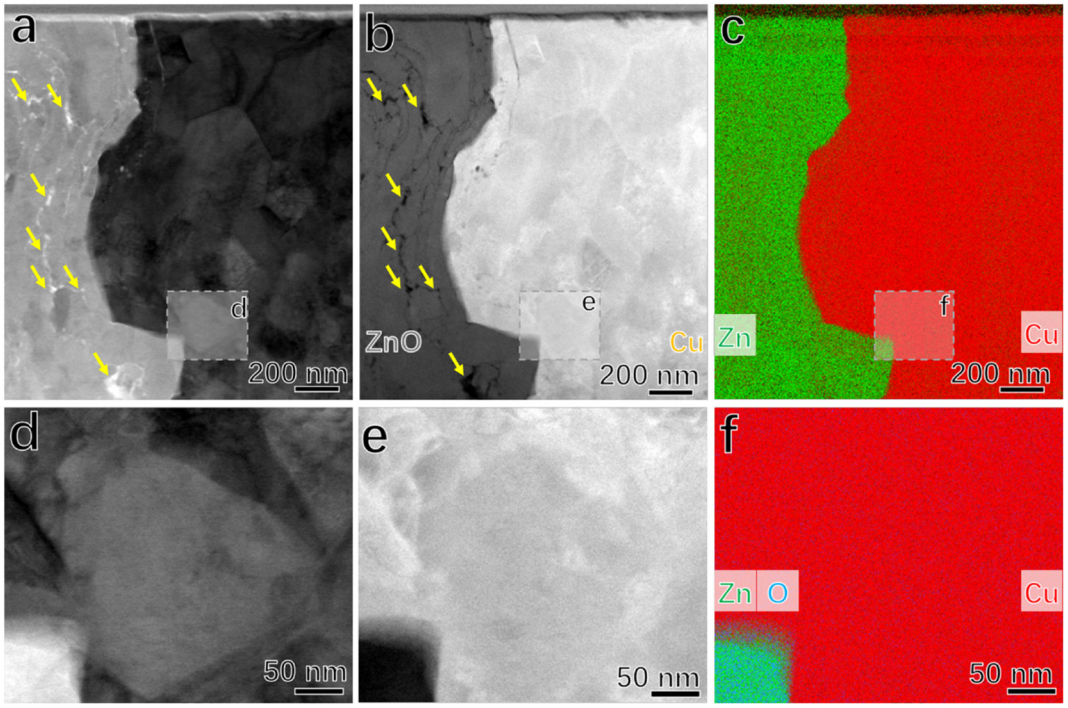

Fig. 10. STEM characterization and EDX mapping of the interface between ZnO cluster and Cu matrix. (a, d) BF-STEM images; (b, e) HAADF images; (c, f) EDX mapping showing Zn, Cu, and O elements distribution. Voids between ZnO particles were highlighted by yellow arrows in (a, b). (For interpretation of the references to color in this figure legend, the reader is referred to the web version of this article.)

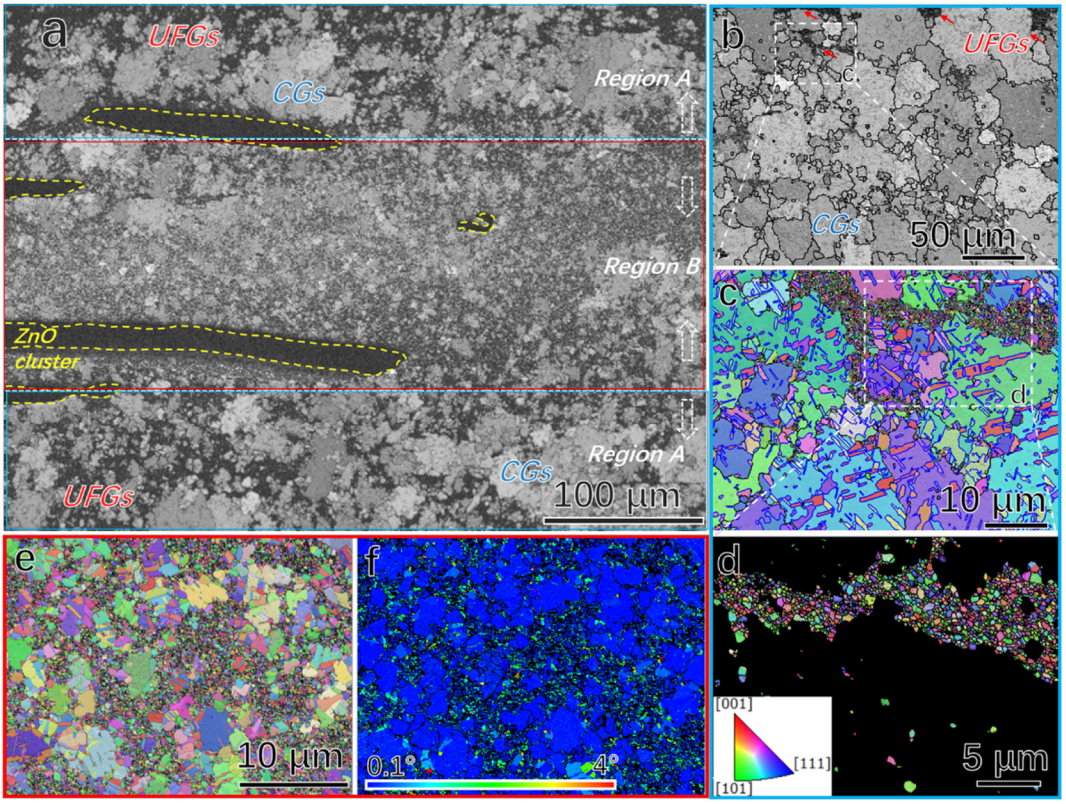

Fig. 11. EBSD maps showing the microstructure of HPT-processed Cu-ZnO disk. (a) Large-area BC image showing the overall microstructure, ZnO clusters (marked by yellow dashed curves), and two regions with low and high relative fraction of UFGs (Regions A and B, respectively). (b–d) are from Region A with increasingly enlarged magnifications and (e, f) are from Region B. UFGs in (c) are subdivided and highlighted in (d). (f) Presents the GOS map of (e). Note the following orientation images use the same legend. (For interpretation of the references to color in this figure legend, the reader is referred to the web version of this article.)

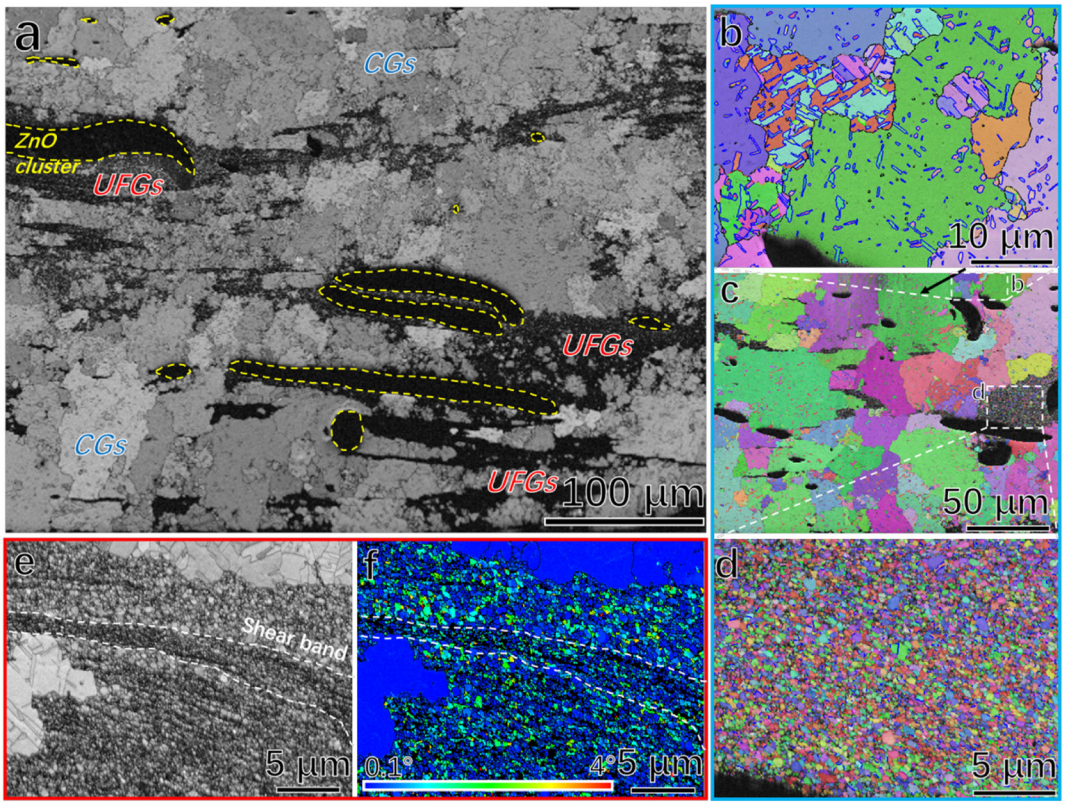

Fig. 12. EBSD maps showing the microstructure of HPT-processed Cu-Holes-ZnO disk. (a) BC image showing the overview of the microstructure; (b–d) orientation maps from one representative region containing CG with twins and UFG clusters; UFGs in (c) are highlighted in (d); (e, f) BC and GOS maps from another representative region exhibiting UFG clusters located at some distance from ZnO clusters.

excessive vacancies and pores drag effect [38]. The GOS map in Fig. 12(f) demonstrate that most UFGs exhibit high defects density and internal strain, whereas the CGs are free of any residual strain and had obviously formed during recrystallization and grain growth.

3.2.3. HPT-processed Cu and Cu-Holes Disks

To evaluate the effect of ZnO clusters and pre-existing holes on the microstructural evolution of Cu matrix, EBSD measurements were also conducted on HPT-processed Cu and Cu-Holes disks. As seen in Fig. 13(a, b), the homogeneous CGs (~5 μm in size) with annealing twins (0.50 ± 0.32 μm in thickness) were found in HPT-processed Cu disk. Similar homogeneous grain coarsening was as found in HPT-processed high purity Ni at 150 °C [55]. On the other hand, the clusters of UFGs (~0.59 μm in size) embedded in the CG matrix (~9 μm in size) were found in the HPT-processed Cu-Holes disk (see Fig. 13(d, e)). We believe that these UFGs were formed at the bonded internal surfaces of the healed pre-existing holes [38]. The GOS maps, Fig. 13(c, f), indicate that CGs and UFGs consistently exhibit low and high values of GOS,

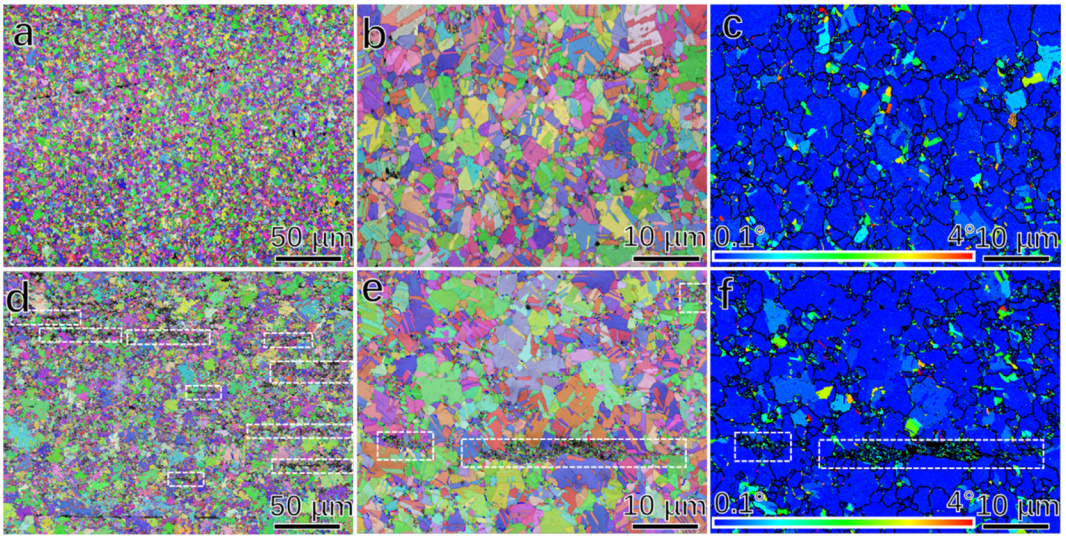

Fig. 13. The orientation and GOS maps of the HPT-processed (a–c) Cu and (d–f) Cu-Holes disks. White dashed boxes in (d, e) highlight the UFG regions embedded in the CG matrix. (c) and (f) are GOS images of (b) and (e), respectively.

respectively.

In summary, the HPT-processed Cu disk exhibits the most uniform grain coarsening during the post-processing handling (holding at ambient conditions and heating at 120 °C for 20 min). By introducing holes, ZnO particles, and both of them together, the abnormal grain growth became increasingly preferred as the ratio of CG to UFG sizes increased from 15 to 80 and 120, respectively. Finally, in all three cases, only partial recovery has occurred in the UFG clusters, since the GOS maps indicated that they still had residual strains.

4. Discussion

In this section, the flow behavior and deagglomeration of ZnO clusters is first considered. Then, the plastic deformation of the ceramic ZnO nanoparticles is analyzed. Lastly, the formation mechanisms of the bimodal microstructure found in Cu matrix are discussed.

4.1. Deagglomeration of ZnO Clusters

Two models have been proposed to describe the morphology evolution of heterogeneous materials caused by shearing instability. They both are based on the concept of hydrodynamic instability. One approach is derived from geological systems, where folding and necking are used to describe the morphological events that occur in rocks on the scale from centimeters to kilometers [56,57]. The occurrences of these two events depend on the effective viscosity ratio between the rocks and the medium they are embedded in [57–59]. The other theory is based on the interaction between the flow of two fluids with different velocities, in which turbulent and laminar flow patterns are used to describe the geometry of the flow [59–62]. High strain gradient and strain rate gradient between different layers are believed to be the reason for the morphological events. In what follows, we will discuss the evolution of ZnO clusters from both perspectives.

In a recent study by Pouryazdan et al. [59], multilayered Al/Cu and Ag/Cu composites were processed by HPT. It has been conjected that the viscosity contrast (VC) between the two phases in the multilayers and stress exponent, n, are two determinant factors that affect the development of the composite microstructure. High VC/n ratio leads to fold formation, while delamination/necking or lamellar flow is dominant in the system with a low VC/n. By adopting this theory in the present study, the fact that fold formation was dominant in the HPT-processed Cu-Holes-ZnO disk could be explained by the higher VC value in this system as compared to that in Cu-ZnO disk. Indeed, the effective viscosity of the Cu disk was decreased by introducing holes, which leaded to an increased VC with ZnO cluster. On the contrary, relatively low VC in the Cu-ZnO system leaded to lamellar flow, necking of ZnO clusters and elongation of ZnO particles. Therefore, it is likely that viscosity contrast affects the morphological evolution of the Cu-ZnO composites.

On the other hand, the UFG layers that formed in Cu at its interface with ZnO clusters (Fig. 8) indicate that shear strain gradients induced by the difference in shear strain rates in the two phases have to be taken into account. In Bachmaier et al. [63] and Sun et al. [17] recent works on the HPT processing of metallic hybrids, it has been found that mechanical alloying and formation of intermetallic phase occurred before the deformation and fracture of the hard phase constituent. This indicates that interface sliding originated from the difference of plastic flow velocities is the dominant factor for chemical intermixing at interfaces. The velocity difference across the interface is one of the key contributing factors for the occurrence of Kelvin-Helmholtz instability. In this theory, the transition between the turbulent flow and laminar flow is determined by the Reynolds number, R_e, above which the flow pattern is turbulent and below which it is laminar.

$$R_e = \frac{\rho v L}{\eta_{eff}}$$

where ρ is the density of Cu (8920 kg m^{-3}), v is the characteristic flow velocity, L is a characteristic linear dimension (5×10^{-3} m), and η_{eff} is the effective viscosity of Cu at hydrodynamic pressure (assuming as low as 10^4 Pa·s). Based on Pouryazdan et al. [59] and our own estimates, to realize the turbulent flow pattern we observed in Cu-Holes-ZnO disk, the plastic flow velocity should be in the km/s range, which is unrealistic even when the “fast” formation of adiabatic shear bands is taken into account. Therefore, the classic Kelvin-Helmholtz instability model cannot be applied here for explaining the ZnO cluster vortices. In summary, the hydrodynamic instability theory established in the geological community can be adopted here to explain the evolution of ZnO clusters. Though the viscosity contrast and stress exponent are the two key factors, our observations indicate that interfacial shear sliding between the two phases also plays some role in the morphological evolution.

Finally, we would like to mention Beygelzimer et al. and Kulagin et al.'s theory about shear mixing under HPT processing [64–67], in which a transition from laminar to turbulent plastic flow was related to the shear blocking by hard inclusions. The hardness of ZnO nanoparticles is higher than that of Cu, which means that the mechanisms considered in Refs. [64–67] may also play a role in the present work.

4.2. Deformation of ZnO Particles

The ZnO ceramic nanoparticles embedded in the Cu matrix underwent unusually high extent of plastic deformation during the HPT processing of the sandwich structure. The large-strain plasticity in intrinsically brittle ceramics has been observed in two cases. In the first case, deformation was usually conducted under hydrostatic confining pressure and at elevated temperature, to facilitate the transformation from micro-cracking to plastic slip for inelastic relaxation, and reduce the critical resolved shear stress for activation of slip systems [68–71]. Recent studies by Amodeo et al. [72] showed that the confining pressure directly affects the electronic structure and bonding of MgO and the core structure and mobility of dislocations. In the second case, deformation was carried out at ambient temperature but on nano-scale ceramic wires/rods, and the brittle fracture was postponed due to the scale-related dislocation activity [73–75]. Also, significant plasticity of intrinsically brittle oxide ceramics was observed in nano- and micro-indentation tests that combine both the hydrostatic compression and the sub-micrometer size effect [76,77]. Hockey demonstrated significant plasticity of sapphire single crystals during microindentation and observed the high density of dislocations and twins in the indented zone [77]. Similarly, the small size of ZnO particles employed in the present work (~350 nm) and very high hydrostatic pressure during HPT (5 GPa) indicate that both extrinsic (deformation conditions) and intrinsic (particle dimensions) factors contributed to the large strain plasticity and high shaping ability of the particles.

It has been recently shown that HPT-induced plastic deformation of ceramic particles changes their functional properties (e.g. bandgap narrowing, photoluminescence, photocatalytic activity and dielectric properties) due to the deformation-induced formation of new phases and oxygen vacancies [78–83]. Theoretical work also proved that combining hydrostatic pressure with shear strain increases the thermodynamic driving force for pressure-induced phase transformation [84]. Razavi-Khosroshahi et al. have observed a phase transformation of ZnO from hexagonal wurtzite to cubic rocksalt phase during the HPT under the pressure of 6 GPa [81]. The HPT pressure employed in this study (5 GPa) was probably below the threshold value for transformation (6 GPa, higher than the hardness of ZnO, 2-5 GPa [44–46]), so that the particles remained in single-phase, wurtzite state.

4.3. Bimodal Grain Distribution in Cu

Our EBSD studies demonstrated that adding of ZnO particles between the two Cu disks, and introducing holes in the Cu disk promote

formation of bimodal microstructure in the Cu matrix after HPT processing and post-processing handling. The Cu disk and Cu-Holes disk processed and handled under identical conditions exhibited more homogeneous CG microstructure, with some isolated UFG clusters in the regions of healed pre-existing holes (Fig. 13e). This uniform and continuous recrystallization and coarsening is related to the fact that at very high strain level the distribution of strain is very homogenous and there are no recognizable "nucleation" and "growth" stages [85,86]. In this classic theory, discontinuous static recrystallization with abnormal grain growth is usually expected in deformed structure with low imposed strain (usually less than 2) and heterogeneous strain distribution [86,87]. In the present case, heterogeneous strain distribution was obtained even after a very high strain was imposed on Cu-ZnO and Cu-Holes-ZnO disks because of the presence of ZnO particles and pre-fabricated holes.

Similar bimodal grain size distribution after annealing of highly strained samples was found in several other studies of nano-reinforced ferritic steel powders after high energy ball milling [88–91]. For example, in Sallez et al. recent study of annealed nanoreinforced steel powder [91], UFG clusters were embedded in CGs and thermally stable even at high temperature close to the solidus temperature (Fig. 11 in Ref. [91]). We assume that large strain gradients in the composite Cu-ZnO samples result in especially potent sites for recrystallization during post-processing handling of the samples [85,86]. The high efficiency of these sites, and their small number result in large size of recrystallized grains. At the same time, the recrystallization front is pushing the residual impurities in the Cu matrix towards the untransformed regions of the UFG matrix. In Cu, such re-distribution of impurities can proceed by grain boundary diffusion even at room or slightly elevated (120 °C) temperatures. As proposed by Prokoshkina et al. [55], the residual impurities accumulating in the untransformed UFG matrix reduce the grain boundary mobility by the solute drag mechanism and stabilize the UFG structure. Since the UFG regions are predominantly located in the vicinity of ZnO clusters (see Fig. 12), some degree of Zn and O segregation at the Cu grain boundaries (below the detection limit of EDX) cannot be excluded. These impurities should provide additional stabilization against the recrystallization and grain growth.

5. Conclusions

We have studied the microstructure evolution in HPT-processed bulk metal (Cu) - ceramic particles (ZnO) hybrid material. The following conclusions can be drawn from the present study:

1. The HPT caused the deagglomeration and fragmentation of ZnO clusters due to the hydrodynamic instabilities associated with the plastic flow in the Cu matrix. Pre-fabricated holes in Cu disks increased the viscosity contrast between the ZnO particles and the Cu matrix, thus increasing the turbulence of the plastic flow and enhancing the deagglomeration and refinement of ZnO clusters.
2. Embedded ZnO particles were plastically deformed to a compressive strain of 86% during HPT in the two studied sandwich structures. In addition, strong basal texture was found in the deformed ZnO clusters. The small size of ZnO particles (~350 nm) and very high hydrostatic pressure during HPT (5 GPa) contributed to the large strain plasticity and high shaping ability of the particles.
3. ZnO powders and pre-fabricated holes caused increased strain gradients in the Cu matrix during the HPT processing. Consequently, this increased the propensity of the UFG Cu matrix for recrystallization and abnormal grain growth. As a result, a bimodal microstructure was formed in the Cu-ZnO hybrids during post-processing samples handling. The increased stability of the residual clusters of UFGs was attributed to re-distribution of impurities during recrystallization and abnormal grain growth.

Data Availability

The experimental procedures required to reproduce these findings are available in the "Experimental methods" section. The EBSD raw data required to reproduce these microstructural findings are available to download from "https://www.dropbox.com/sh/tjgesbzxiiq81n9/AACzv_8HzE3gk6FGwg7RcN1Ea?dl=0".

Acknowledgements

The authors gratefully acknowledge the technical assistance provided by the staff of Electron Microscopy Center at the Department of Mater Sci Eng (Dr. Y. Kauffmann, Dr. A. Berner, and Mr. M. Kalina), and of the FIB laboratory of the Russell Berrie Nanotechnology Institute, Technion (Dr. G. Attiya). The work was supported by the Ministry of Science & Technology, Israel (grant 3-12418), Ministry of Education and Science of the Russian Federation in the framework of the Program to Increase the Competitiveness of NUST "MISiS", and by Russian Foundation for Basic Research (grant 15-53-06008). YQ would like to thank the support by Technion-Guangdong Postdoctoral Fellowship.

References

[1] G. Wu, K.C. Chan, L. Zhu, L. Sun, J. Lu, Dual-phase nanostructuring as a route to high-strength magnesium alloys, Nature 545 (2017) 80–83.
[2] X. Li, K. Lu, Playing with defects in metals, Nat. Mater. 16 (2017) 700.
[3] X. Wu, Y. Zhu, Heterogeneous materials: a new class of materials with unprecedented mechanical properties, Mater. Res. Lett. 5 (2017) 527–532.
[4] O. Bouaziz, H.S. Kim, Y. Estrin, Architecturing of metal-based composites with concurrent nanostructuring: a new paradigm of materials design, Adv. Eng. Mater. 15 (2013) 336–340.
[5] D. Raabe, P.P. Choi, Y. Li, A. Kostka, X. Sauvage, F. Lecouturier, K. Hono, R. Kirchheim, R. Pippan, D. Embury, Metallic composites processed via extreme deformation: toward the limits of strength in bulk materials, MRS Bull. 35 (2010) 982–991.
[6] W. Xing, A.R. Kalidindi, C.A. Schuh, Preferred nanocrystalline configurations in ternary and multicomponent alloys, Scr. Mater. 127 (2017) 136–140.
[7] E. Ma, T. Zhu, Towards strength–ductility synergy through the design of heterogeneous nanostructures in metals, Mater. Today 20 (2017) 323–331.
[8] X. Wu, P. Jiang, L. Chen, F. Yuan, Y.T. Zhu, Extraordinary strain hardening by gradient structure, Proc. Natl. Acad. Sci. U. S. A. 111 (2014) 7197–7201.
[9] O. Bouaziz, Y. Brechet, J.D. Embury, Heterogeneous and architectured materials: a possible strategy for design of structural materials, Adv. Eng. Mater. 10 (2008) 24–36.
[10] R. Lapovok, Y. Qi, H.P. Ng, V. Maier, Y. Estrin, Multicomponent materials from machining chips compacted by equal-channel angular pressing, J. Mater. Sci. 49 (2014) 1193–1204.
[11] Y. Qi, K.G. Contreras, H.D. Jung, H.E. Kim, R. Lapovok, Y. Estrin, Ultrafine-grained porous titanium and porous titanium/magnesium composites fabricated by space holder-enabled severe plastic deformation, Mater. Sci. Eng. C 59 (2016) 754–765.
[12] Y. Qi, R. Lapovok, Y. Estrin, Microstructure and electrical conductivity of aluminium/steel bimetallic rods processed by severe plastic deformation, J. Mater. Sci. 51 (2016) 6860–6875.
[13] X. Sauvage, F. Wetscher, P. Pareige, Mechanical alloying of Cu and Fe induced by severe plastic deformation of a Cu–Fe composite, Acta Mater. 53 (2005) 2127–2135.
[14] A. Bachmaier, M. Kerber, D. Setman, R. Pippan, The formation of supersaturated solid solutions in Fe–Cu alloys deformed by high-pressure torsion, Acta Mater. 60 (2012) 860–871.
[15] K. Edalati, S. Toh, H. Iwaoka, Z. Horita, Microstructural characteristics of tungsten-base nanocomposites produced from micropowders by high-pressure torsion, Acta Mater. 60 (2012) 3885–3893.
[16] K. Oh-ishi, K. Edalati, H.S. Kim, K. Hono, Z. Horita, High-pressure torsion for enhanced atomic diffusion and promoting solid-state reactions in the aluminum–copper system, Acta Mater. 61 (2013) 3482–3489.
[17] Y. Sun, M. Aindow, R.J. Hebert, T.G. Langdon, E.J. Lavernia, High-pressure torsion-induced phase transformations and grain refinement in Al/Ti composites, J. Mater. Sci. 52 (2017) 12170–12184.
[18] Y. Sun, H. Fujii, T. Nakamura, N. Tsuji, D. Todaka, M. Umemoto, Critical strain for mechanical alloying of Cu–Ag, Cu–Ni and Cu–Zr by high-pressure torsion, Scr. Mater. 65 (2011) 489–492.
[19] M. Kawasaki, B. Ahn, H. Lee, A.P. Zhilyaev, T.G. Langdon, Using high-pressure torsion to process an aluminum–magnesium nanocomposite through diffusion bonding, J. Mater. Res. 31 (2016) 88–99.
[20] B. Ahn, H.J. Lee, I.C. Choi, M. Kawasaki, J.I. Jang, T.G. Langdon, Micro-mechanical behavior of an exceptionally strong metal matrix nanocomposite processed by high-pressure torsion, Adv. Eng. Mater. 18 (2016) 1001–1008.
[21] B. Ahn, A.P. Zhilyaev, H.J. Lee, M. Kawasaki, T.G. Langdon, Rapid synthesis of an extra hard metal matrix nanocomposite at ambient temperature, Mater. Sci. Eng. A

635 (2015) 109–117.
[22] J.K. Han, H.J. Lee, J.I. Jang, M. Kawasaki, T.G. Langdon, Micro-mechanical and tribological properties of aluminum-magnesium nanocomposites processed by high-pressure torsion, Mater. Sci. Eng. A 684 (2017) 318–327.
[23] S.O. Rogachev, S.A. Nikulin, A.B. Rozhnov, V.M. Khatkevich, T.A. Nechaykina, M.V. Gorshenkov, R.V. Sundeev, Multilayer "steel/vanadium alloy/steel" hybrid material obtained by high-pressure torsion at different temperatures, Metall. Mater. Trans. A 48 (2017) 6091–6101.
[24] N. Ibrahim, M. Peterlechner, F. Emeis, M. Wegner, S.V. Divinski, G. Wilde, Mechanical alloying via high-pressure torsion of the immiscible $Cu_{50}Ta_{50}$ system, Mater. Sci. Eng. A 685 (2017) 19–30.
[25] X. Sauvage, G.P. Dinda, G. Wilde, Non-equilibrium intermixing and phase transformation in severely deformed Al/Ni multilayers, Scr. Mater. 56 (2007) 181–184.
[26] A. Mendes, I. Timokhina, A. Molotnikov, P.D. Hodgson, R. Lapovok, Role of shear in interface formation of aluminium-steel multilayered composite sheets, Mater. Sci. Eng. A 705 (2017) 142–152.
[27] H.P. Ng, T. Przybilla, C. Schmidt, R. Lapovok, D. Orlov, H.-W. Höppel, M. Göken, Asymmetric accumulative roll bonding of aluminium–titanium composite sheets, Mater. Sci. Eng. A 576 (2013) 306–315.
[28] X. Ma, C. Huang, J. Moering, M. Ruppert, H.W. Höppel, M. Göken, J. Narayan, Y. Zhu, Mechanical properties of copper/bronze laminates: role of interfaces, Acta Mater. 116 (2016) 43–52.
[29] Z. Wang, J. Perepezko, D. Larson, D. Reinhard, Intermixing in Cu/Ni multilayers induced by cold rolling, J. Appl. Phys. 117 (2015) 165902.
[30] Y. Estrin, A. Vinogradov, Extreme grain refinement by severe plastic deformation: a wealth of challenging science, Acta Mater. 61 (2013) 782–817.
[31] K. Edalati, H. Iwaoka, Z. Horita, M. Konno, T. Sato, Unusual hardening in Ti/Al_2O_3 nanocomposites produced by high-pressure torsion followed by annealing, Mater. Sci. Eng. A 529 (2011) 435–441.
[32] A. Mazilkin, G. Abrosimova, S. Protasova, B. Straumal, G. Schütz, S. Dobatkin, A. Bakai, Transmission electron microscopy investigation of boundaries between amorphous "grains" in $Ni_{50}Nb_{20}Y_{30}$ alloy, J. Mater. Sci. 46 (2011) 4336–4342.
[33] B.B. Straumal, A.A. Mazilkin, B. Baretzky, G. Schütz, E. Rabkin, R.Z. Valiev, Accelerated diffusion and phase transformations in Co–Cu alloys driven by the severe plastic deformation, Mater. Trans. 53 (2012) 63–71.
[34] B.B. Straumal, V. Pontikis, A. Kilmametov, A. Mazilkin, S. Dobatkin, B. Baretzky, Competition between precipitation and dissolution in Cu–Ag alloys under high pressure torsion, Acta Mater. 122 (2017) 60–71.
[35] B.B. Straumal, A.R. Kilmametov, Y. Ivanisenko, A.A. Mazilkin, O.A. Kogtenkova, L. Kurmanaeva, A. Korneva, P. Zięba, B. Baretzky, Phase transitions induced by severe plastic deformation: steady-state and equifinality, Int. J. Mater. Res. 106 (2015) 657–664.
[36] B. Straumal, A. Kilmametov, A. Korneva, A. Mazilkin, P. Straumal, P. Zięba, B. Baretzky, Phase transitions in Cu-based alloys under high pressure torsion, J. Alloys Compd. 707 (2017) 20–26.
[37] S. Kattel, P.J. Ramírez, J.G. Chen, J.A. Rodriguez, P. Liu, Active sites for CO_2 hydrogenation to methanol on Cu/ZnO catalysts, Science 355 (2017) 1296–1299.
[38] Y. Qi, A. Kosinova, E. Rabkin, A.R. Kilmametov, B. Straumal, Generation and healing of porosity in high purity copper by high-pressure torsion, Mater. Charact. 145 (2018) 1–9.
[39] M. Kawasaki, Different models of hardness evolution in ultrafine-grained materials processed by high-pressure torsion, J. Mater. Sci. 49 (2014) 18–34.
[40] T.G. Langdon, Twenty-five years of ultrafine-grained materials: achieving exceptional properties through grain refinement, Acta Mater. 61 (2013) 7035–7059.
[41] R.Z. Valiev, Y.V. Ivanisenko, E.F. Rauch, B. Baudelet, Structure and deformaton behaviour of Armco iron subjected to severe plastic deformation, Acta Mater. 44 (1996) 4705–4712.
[42] R. Lapovok, H.P. Ng, D. Tomus, Y. Estrin, Bimetallic copper–aluminium tube by severe plastic deformation, Scr. Mater. 66 (2012) 1081–1084.
[43] A. Moezzi, A.M. McDonagh, M.B. Cortie, Zinc oxide particles: synthesis, properties and applications, Chem. Eng. J. 185 (2012) 1–22.
[44] S. Basu, M.W. Barsoum, Deformation micromechanisms of ZnO single crystals as determined from spherical nanoindentation stress–strain curves, J. Mater. Res. 22 (2007) 2470–2477.
[45] V. Coleman, J. Bradby, C. Jagadish, P. Munroe, Y. Heo, S. Pearton, D. Norton, M. Inoue, M. Yano, Mechanical properties of ZnO epitaxial layers grown on a-and c-axis sapphire, Appl. Phys. Lett. 86 (2005) 203105.
[46] S. Kucheyev, J. Bradby, J. Williams, C. Jagadish, M. Swain, Mechanical deformation of single-crystal ZnO, Appl. Phys. Lett. 80 (2002) 956–958.
[47] P. Cordier, J. Amodeo, P. Carrez, Modelling the rheology of MgO under Earth's mantle pressure, temperature and strain rates, Nature 481 (2012) 177.
[48] I. Issa, J. Amodeo, J. Réthoré, L. Joly-Pottuz, C. Esnouf, J. Morthomas, M. Perez, J. Chevalier, K. Masenelli-Varlot, In situ investigation of MgO nanocube deformation at room temperature, Acta Mater. 86 (2015) 295–304.
[49] J. Amodeo, P. Carrez, B. Devincre, P. Cordier, Multiscale modelling of MgO plasticity, Acta Mater. 59 (2011) 2291–2301.
[50] J. Amodeo, S. Dancette, L. Delannay, Atomistically-informed crystal plasticity in MgO polycrystals under pressure, Int. J. Plast. 82 (2016) 177–191.
[51] P. Lin, X. Du, Y. Chen, H. Chen, J. Huang, Nano-scaled diffusional or dislocation creep analysis of single-crystal ZnO, AIP Adv. 6 (2016) 095125.
[52] S.-R. Jian, Pop-in effects and dislocation nucleation of c-plane single-crystal ZnO by Berkovich nanoindentation, J. Alloys Compd. 644 (2015) 54–58.
[53] H. Jiang, Y.T. Zhu, D.P. Butt, I.V. Alexandrov, T.C. Lowe, Microstructural evolution, microhardness and thermal stability of HPT-processed Cu, Mater. Sci. Eng. A 290 (2000) 128–138.
[54] Y. Huang, S. Sabbaghianrad, A.I. Almazrouee, K.J. Al-Fadhalah, S.N. Alhajeri, T.G. Langdon, The significance of self-annealing at room temperature in high purity copper processed by high-pressure torsion, Mater. Sci. Eng. A 656 (2016) 55–66.
[55] D. Prokoshkina, L. Klinger, A. Moros, G. Wilde, E. Rabkin, S.V. Divinski, Persistence of ultrafast atomic diffusion paths in recrystallizing ultrafine grained Ni, Scr. Mater. 101 (2015) 91–94.
[56] M. von Tscharner, S. Schmalholz, A 3-D Lagrangian finite element algorithm with remeshing for simulating large-strain hydrodynamic instabilities in power law viscoelastic fluids, Geochem. Geophys. Geosyst. 16 (2015) 215–245.
[57] S.M. Schmalholz, N.S. Mancktelow, Folding and necking across the scales: a review of theoretical and experimental results and their applications, Solid Earth 7 (2016) 1417.
[58] Y. Estrin, R. Kulagin, Y. Beygelzimer, Think big, manufacture small: microfabrication on a desktop by severe plastic deformation, Mater. Today (2017) https://www.materialstoday.com/surface-science/comment/think-big-manufacture-small/ (accessed 3 September 2018).
[59] M. Pouryazdan, B.J. Kaus, A. Rack, A. Ershov, H. Hahn, Mixing instabilities during shearing of metals, Nat. Commun. 8 (2017) 1611.
[60] N.K. Sundaram, Y. Guo, S. Chandrasekar, Mesoscale folding, instability, and disruption of laminar flow in metal surfaces, Phys. Rev. Lett. 109 (2012) 106001.
[61] Z.-P. Luo, G.-P. Zhang, R. Schwaiger, Microstructural vortex formation during cyclic sliding of Cu/Au multilayers, Scr. Mater. 107 (2015) 67–70.
[62] D.A. Rigney, S. Karthikeyan, The evolution of tribomaterial during sliding: a brief introduction, Tribol. Lett. 39 (2010) 3–7.
[63] K.S. Kormout, R. Pippan, A. Bachmaier, Deformation-induced supersaturation in immiscible material systems during high-pressure torsion, Adv. Eng. Mater. 19 (2017).
[64] Y. Beygelzimer, Vortices and mixing in metals during severe plastic deformation, Mater Sci Forum, Trans Tech Publ, 2011, pp. 213–224.
[65] Y. Beygelzimer, R. Valiev, V. Varyukhin, Simple shear: double-stage deformation, Mater Sci Forum, Trans Tech Publ, 2011, pp. 97–102.
[66] R. Kulagin, Y. Beygelzimer, Y. Ivanisenko, A. Mazilkin, H. Hahn, High pressure torsion: from laminar flow to turbulence, IOP Conference Series: Mater Sci Eng, IOP Publishing, 2017, p. 012045.
[67] R. Kulagin, Y. Beygelzimer, Y. Ivanisenko, A. Mazilkin, B. Straumal, H. Hahn, Instabilities of interfaces between dissimilar metals induced by high pressure torsion, Mater. Lett. 222 (2018) 172–175.
[68] V.S. Deshpande, A.G. Evans, Inelastic deformation and energy dissipation in ceramics: a mechanism-based constitutive model, J. Mech. Phys. Solids 56 (2008) 3077–3100.
[69] K.P.D. Lagerlöf, A.H. Heuer, J. Castaing, J.P. Riviere, T.E. Mitchell, Slip and twinning in sapphire (α-Al_2O_3), J. Am. Ceram. Soc. 77 (1994) 385–397.
[70] M. Klassen-Neklyudova, Plastic deformation of crystals of synthetic corundum, J. Tech. Phys. 12 (519–34) (1942) 535–551.
[71] J. Wachtman Jr., I. Maxwell, Plastic deformation of ceramic-oxide single crystals, J. Am. Ceram. Soc. 37 (7) (1954) 291–299.
[72] J. Amodeo, P. Carrez, P. Cordier, Modelling the effect of pressure on the critical shear stress of MgO single crystals, Philos. Mag. 92 (2012) 1523–1541.
[73] X. Han, Y. Zhang, K. Zheng, X. Zhang, Z. Zhang, Y. Hao, X. Guo, J. Yuan, Z. Wang, Low-temperature in situ large strain plasticity of ceramic SiC nanowires and its atomic-scale mechanism, Nano Lett. 7 (2007) 452–457.
[74] M. Riaz, A. Fulati, L. Yang, O. Nur, M. Willander, P. Klason, Bending flexibility, kinking, and buckling characterization of ZnO nanorods/nanowires grown on different substrates by high and low temperature methods, J. Appl. Phys. 104 (2008) 104306.
[75] J. Karch, R. Birringer, H. Gleiter, Ceramics ductile at low temperature, Nature 330 (1987) 556–558.
[76] A.C. Fischer-Cripps, A simple phenomenological approach to nanoindentation creep, Mater. Sci. Eng. A 385 (2004) 74–82.
[77] B.J. Hockey, Plastic deformation of aluminum oxide by indentation and abrasion, J. Am. Ceram. Soc. 54 (1971) 223–231.
[78] K. Edalati, Review on recent advancements in severe plastic deformation of oxides by high-pressure torsion (HPT), Adv. Eng. Mater. (2018) 1800272, , https://doi.org/10.1002/adem.201800272.
[79] I. Fujita, K. Edalati, X. Sauvage, Z. Horita, Grain growth in nanograined aluminum oxide by high-pressure torsion: phase transformation and plastic strain effects, Scr. Mater. 152 (2018) 11–14.
[80] H. Razavi-Khosroshahi, K. Edalati, H. Emami, E. Akiba, Z. Horita, M. Fuji, Optical properties of nanocrystalline monoclinic Y_2O_3 stabilized by grain size and plastic strain effects via high-pressure torsion, Inorg. Chem. 56 (2017) 2576–2580.
[81] H. Razavi-Khosroshahi, K. Edalati, J. Wu, Y. Nakashima, M. Arita, Y. Ikoma, M. Sadakiyo, Y. Inagaki, A. Staykov, M. Yamauchi, High-pressure zinc oxide phase as visible-light-active photocatalyst with narrow band gap, J. Mater. Chem. A 5 (2017) 20298–20303.
[82] K. Edalati, M. Arimura, Y. Ikoma, T. Daio, M. Miyata, D.J. Smith, Z. Horita, Plastic deformation of $BaTiO_3$ ceramics by high-pressure torsion and changes in phase transformations, optical and dielectric properties, Mater. Res. Lett. 3 (2015) 216–221.
[83] H. Razavi-Khosroshahi, K. Edalati, M. Arita, Z. Horita, M. Fuji, Plastic strain and grain size effect on high-pressure phase transformations in nanostructured TiO_2 ceramics, Scr. Mater. 124 (2016) 59–62.
[84] V.I. Levitas, M. Javanbakht, Phase transformations in nanograin materials under high pressure and plastic shear: nanoscale mechanisms, Nanoscale 6 (2014) 162–166.
[85] F.J. Humphreys, M. Hatherly, Recrystallization and Related Annealing Phenomena, Elsevier, 2012.
[86] T. Sakai, A. Belyakov, R. Kaibyshev, H. Miura, J.J. Jonas, Dynamic and post-

dynamic recrystallization under hot, cold and severe plastic deformation conditions, Prog. Mater. Sci. 60 (2014) 130–207.
[87] V.M. Miller, A.E. Johnson, C.J. Torbet, T.M. Pollock, Recrystallization and the development of abnormally large grains after small strain deformation in a polycrystalline nickel-based superalloy, Metall. Mater. Trans. A 47 (2016) 1566–1574.
[88] X. Boulnat, M. Perez, D. Fabregue, T. Douillard, M.-H. Mathon, Y. De Carlan, Microstructure evolution in nano-reinforced ferritic steel processed by mechanical alloying and spark plasma sintering, Metall. Mater. Trans. A 45 (2014) 1485–1497.
[89] X. Boulnat, N. Sallez, M. Dadé, A. Borbély, J.L. Béchade, Y. de Carlan, J. Malaplate, Y. Bréchet, F. de Geuser, A. Deschamps, P. Donnadieu, D. Fabrègue, M. Perez, Influence of oxide volume fraction on abnormal growth of nanostructured ferritic steels during non-isothermal treatments: an in situ study, Acta Mater. 97 (2015) 124–130.
[90] E. Aydogan, O. El-Atwani, S. Takajo, S.C. Vogel, S.A. Maloy, High temperature microstructural stability and recrystallization mechanisms in 14YWT alloys, Acta Mater. 148 (2018) 467–481.
[91] N. Sallez, X. Boulnat, A. Borbély, J.L. Béchade, D. Fabrègue, M. Perez, Y. de Carlan, L. Hennet, C. Mocuta, D. Thiaudière, Y. Bréchet, In situ characterization of microstructural instabilities: recovery, recrystallization and abnormal growth in nanoreinforced steel powder, Acta Mater. 87 (2015) 377–389.